




# Microstructural and mechanical characterization of $\text{Na}_{1+x}\text{Hf}_2\text{Si}_{2.3}\text{P}_{0.7}\text{O}_{10.85+0.5x}$ and $\text{Na}_{1+x}\text{Zr}_2\text{P}_{3-x}\text{Si}_x\text{O}_{12}$ NASICON-type solid electrolytes

Jürgen Peter Gross<sup>1,\*</sup> , Gerald Dück<sup>2</sup>, Frank Schäfer<sup>3</sup>, Michael Holzapfel<sup>3</sup>, Martin Finsterbusch<sup>2</sup>, Jürgen Malzbender<sup>1</sup>, and Ruth Schwaiger<sup>1,4</sup>

<sup>1</sup>Institute of Energy and Climate Research, Microstructure and Properties of Materials (IEK-2), Forschungszentrum Jülich GmbH, 52425 Jülich, Germany

<sup>2</sup>Institute of Energy and Climate Research, Materials Synthesis and Processing (IEK-1), Forschungszentrum Jülich GmbH, 52425 Jülich, Germany

<sup>3</sup>Fraunhofer-Institute for Chemical Technology (ICT), 76327 Pfinztal, Germany

<sup>4</sup>Chair of Energy Engineering Materials, Faculty 5, RWTH Aachen University, 52056 Aachen, Germany

Received: 23 August 2022

Accepted: 27 November 2022

Published online:

14 December 2022

© The Author(s) 2022

## ABSTRACT

NASICON-type solid electrolytes are promising materials for novel solid-state-batteries aiming toward high energy densities.  $\text{Na}_{1+x}\text{Hf}_2\text{Si}_{2.3}\text{P}_{0.7}\text{O}_{10.85+0.5x}$  with varying sodium content as well as Sc- or Mg-doped and undoped  $\text{Na}_{1+x}\text{Zr}_2\text{P}_{3-x}\text{Si}_x\text{O}_{12}$  were synthesized by solution-assisted solid-state reaction. Microstructural and mechanical characteristics as well as conductivities were investigated. The electrochemical and microstructural properties of all studied materials appear to be highly affected by the sodium content glassy phase and secondary phase formation as well as bloating. The mechanical properties of the specimens depend mainly on microstructural characteristics. Our findings indicate improved mechanical behavior is achieved when bloating and secondary phase formation are inhibited. However, possible influences of glassy phase content on the material properties need to be further investigated.

## Introduction

Renewable energy production is associated with fluctuations that require as one option the integration of low-cost battery storage systems, into the electrical grid [1–3]. Battery storage systems requirements are

long lifetime and high safety. Currently, because of high energy density and long service life, Li-ion batteries are widely used for energy storage; however, they do not fulfill necessary boundary conditions for the stabilization of an energy grid [4]. Thus, alternative batteries are required for large scale stationary storage [5]. Sodium batteries are promising

Handling Editor: David Cann.

Address correspondence to E-mail: j.gross@fz-juelich.de

candidates in this respect, due to the high abundance of sodium, low cost of sodium-containing precursors and high theoretical energy densities compared to other storage technologies, such as redox-flow batteries or compressed gas storage [6–8]. Additionally, issues commonly observed for commercial Li-ion batteries, such as dendrite growth and fire hazards, can be avoided when solid electrolytes such as NASICON ( $\text{Na}^+$  superionic conductors)-type materials, are used [9, 10]. This large family of materials has a stoichiometry of  $\text{Na}_{1+x}\text{Zr}_2\text{Si}_x\text{P}_{3-x}\text{O}_{12}$  ( $0 < x < 3$ ), with  $\text{Na}_3\text{Zr}_2\text{Si}_2\text{PO}_{12}$  (NZSP) being the most common formulation [11]. NASICONs possess high flexibility toward cation-substitution, high chemical stability and ion conductivity competitive to or even surpassing conventional  $\beta''$ -alumina [12]. In general, total ionic conductivities of more than 1 mS/cm have already been reported for certain NASICON compositions [18]. Hence, the materials have been the focus of a significant number of studies [14], the majority of them focusing on the synthesis and conductivity optimization [15–18]. Based on these studies, Mg- and Sc-doped NZSP as well as Hf-containing NASICON with the general formulation  $\text{Na}_{3.0+x}\text{Hf}_2\text{Si}_{2.3}\text{P}_{0.7}\text{O}_{10.85+0.5x}$  (NHSP) emerged as promising materials, due to their high ionic conductivities [19–21].

Complementary investigations regarding the mechanical behavior are rather limited [22]. For Li-ion batteries, the mechanical behavior appears to be affected by the formation and growth of Li-dendrites, leading eventually to material failure [23]. Similarly, for Na-ion batteries, Na filaments have been reported, that lead to material damage and consequently battery failure [24]. Furthermore, other solid-state battery degradation mechanisms, such as crack propagation and contact loss, can be directly linked to the mechanical and microstructural characteristics of the components [25, 26]. It has been suggested, that the critical current density increases with increasing fracture toughness values of the used solid electrolyte [27]. Thus, an optimization of the mechanical and microstructural properties of sodium batteries appears as a promising strategy to improve the failure resilience of the materials [28]. The microstructural properties, such as grain size, secondary phases, glass phases as well as porosity, are suggested to strongly affect the total ionic conductivity [29, 30]. The sintering temperature as well as the sodium content is especially relevant in this respect, since

elevated sintering temperatures and low sodium contents have been reported to lead to secondary  $\text{ZrO}_2$  phases, glass phases, the evaporation of sodium and bloating [31–33].

In the current study,  $\text{Na}_{1+x}\text{Hf}_2\text{Si}_{2.3}\text{P}_{0.7}\text{O}_{10.85+0.5x}$  (NHSP) with varying sodium content as well as Sc- and Mg-doped and undoped  $\text{Na}_{1+x}\text{Zr}_2\text{P}_{3-x}\text{Si}_x\text{O}_{12}$  (NZSP) were synthesized by solution-assisted solid-state reaction and investigated with respect to their microstructures, mechanical properties and conductivities, aiming toward materials' optimization.

## Experimental

The NHSP samples were synthesized analogous to [34–36] by a solution-assisted solid-state-reaction (SA-SSR). Briefly, stoichiometric amounts of  $\text{Na}_2\text{SiO}_3$  (ACS, Merck),  $\text{HfO}(\text{NO}_3)_2 \cdot x \text{H}_2\text{O}$  (99%, Sigma-Aldrich) and  $\text{NH}_4\text{H}_2\text{PO}_4$  ( $\geq 98\%$  Alfa-Aesar) were dissolved in deionized water. Subsequently, tetraethyl-orthosilicate ( $\geq 99\%$ , Sigma-Aldrich) was added to the solution. Using small doses of  $\text{HNO}_3$  (ADC grade, Sigma-Aldrich), the pH value was adjusted to  $\sim 3$ , and all compounds were, thus, fully hydrolyzed. The resulting gel was dried at  $80^\circ\text{C}$  and subsequently calcined at  $750^\circ\text{C}$  for 4 h. The obtained powder was milled in isopropanol using a tumbling mixer (PULVERISETTE 7, Fritsch GmbH, Idar-Oberstein, Germany) with a 50:50 weight-ratio of 3 and 5 mm zirconia balls for approximately 72 h.

The NZSP specimens were also synthesized by the SA-SSR. Stoichiometric amounts of  $\text{NaNO}_3$  (ACS, Merck, Darmstadt, Germany) and  $\text{ZrO}(\text{NO}_3)_2 \cdot x \text{H}_2\text{O}$  (techn. grade, Sigma-Aldrich, St. Louis, USA) were dissolved in deionized water with small amounts of  $\text{HNO}_3$  (ACS, Aldrich) to adjust to a pH of approximately 3. Afterward, tetraethyl-orthosilicate (reagent grade, Merck, Darmstadt, Germany) was added and left to fully hydrolyze before adding  $\text{NH}_4\text{H}_2\text{PO}_4$  (ACS, Merck, Darmstadt, Germany). The resulting gel was dried at  $80^\circ\text{C}$  and calcined at  $800^\circ\text{C}$  for 4 h. After calcination, the powder was also ball-milled in ethanol with a 50:50 weight ratio of 3 and 5 mm zirconia balls for approximately 72 h.

For the synthesis of  $\text{Na}_{3.4}\text{Sc}_{0.4}\text{Zr}_{1.6}\text{Si}_2\text{P}_1\text{O}_{12}$ , a stoichiometric amount of  $\text{Sc}_2\text{O}_3$  (99.5%, Projector GmbH, Duisburg, Germany) was first dissolved in 65%- $\text{HNO}_3$ -solution (ACS, Aldrich), before continuing with the synthesis as described above. Furthermore,

$\text{Na}_{3.1}\text{Mg}_{0.05}\text{Zr}_{1.95}\text{Si}_2\text{P}_1\text{O}_{12}$  was synthesized by adding an appropriate amount of  $\text{Mg}(\text{NO}_3)_2$  (for analysis, Merck, Darmstadt, Germany) to the solution together with the other nitrates, again, synthesis continuing as described above.

The chemical compositions of the materials were determined by inductively coupled plasma–optical emission spectroscopy (ICP-OES) (Thermo Scientific iCAP7600 spectrometer with optical scale and CID semi-conductor detector, axial and radial reflection, wavelength 166–847 nm). Two samples of 50 g each were, together with 0.25 g of lithium borate, transferred to a melt in a platinum crucible followed by heat treatment at 1000 °C for 30 min. The resulting materials were then dissolved in 30 mL of 5%-HCl solution. After the addition of 2 mL HF, the solution was topped up with  $\text{H}_2\text{O}$  to 50 mL of total volume. Two aliquots of each sample were measured in 1/100 and 1/10 dilution. The particle size distributions of the synthesized powders were checked by a laser granulometry instrument (Horiba LA 950 V2, Lier, Belgium) using the Mie scattering theory [37].

The final powders were then pressed into pellets using a uniaxial press (PW 10, P-O-Weber, Remshalden, Germany) with 100 MPa pressure for the NZSP and 190 MPa for the NHSP specimens. The obtained pellets were then sintered at temperatures close to the melting point of the individual compositions in order to achieve good densification; the specific values are stated in Table 1.

In order to prepare them for the subsequent analysis, the pellets were dry-polished by hand using SiC sandpaper (P400 Grit) to obtain flat and parallel surfaces. The specimens were then analyzed by means of X-ray diffraction analysis (XRD) using an EMPYREAN diffractometer (PANalytical, Kassel, Germany), with a Cu-LFF-tube operated at 40 kV and 40 mA. The measurement was taken in the  $2\theta$ -range of 5° to 90°, with a step size of 0.026° and a dwell time per step of 2 s. The resulting XRD patterns were analyzed by Rietveld refinement using the software TOPAS (Bruker AXS, Karlsruhe, Germany).

The samples were sputtered with gold on both sides and placed into an electrochemical cell (Swagelok cell, Düsseldorf, Germany) to measure the ionic conductivity in air at room temperature (20° C) by electrochemical impedance spectroscopy (VMP-300 and SP200, Bio-Logic, France), with an AC frequency range from 3 MHz to 1 Hz and a voltage of 10 mV.

**Table 1** Sinter parameters used for the individual specimens

Specimen	Sintering temperature [°C]	Sintering duration [h]
NZSP3.6	1260	6
NZSP3.0	1260	6
NZScSP	1260	6
NZMgSP	1260	6
NHSP 2.1	1280	5
NHSP 2.3	1280	5
NHSP 2.8	1350	5
NHSP 3.2	1350	5

Sintering temperature values below the melting point of the corresponding compositions were used

Furthermore, samples were cut in half and embedded in epoxy (Epoxy 2000, Cloeren Technology, Wegberg, Germany) for cross-section analysis. The embedded samples were ground with SiC sandpaper and polished with water-free diamond suspension (with grain size of 6  $\mu\text{m}$ , 3  $\mu\text{m}$ , 1  $\mu\text{m}$ ) and then silica suspension (with 0.2  $\mu\text{m}$  grain size) (Cloeren Technology, Wegberg, Germany).

Scanning electron microscopy (SEM) images were obtained using a field emission scanning electron microscope (FE-SEM, MERLIN™, Carl Zeiss Microscopy, Oberkochen, Germany). Elemental analysis of the phases was conducted by energy-dispersive X-ray spectroscopy (EDX) with the X-Max Extreme detector (Oxford Instruments, High Wycombe, UK). Porosity and glassy-content estimations were also carried out based on the analysis of SEM images using ImageJ [38]. The grain size was determined based on the mean linear intercept method following ASTM E112.

Micro-indentation was used to determine the elastic modulus  $E$  and hardness  $H$  using a FISCHERSCOPE® HC 100 instrument (Helmut Fischer GmbH, Sindelfingen, Germany). The experiments were conducted in a load-controlled mode, with loads of 100, 250 and 500 mN. For each load at least 100 individual indents were performed. The indents were performed using a Vickers diamond tip, with a load application time of 15 s. Following the standard DIN EN ISO 3452-1, the  $E$  and  $H$  values were determined from the unloading slope of the load–displacement curve [39]. A Poisson ratio of 0.27 was assumed for the investigated materials [40].

Vickers indentation fracture (VIF) tests were performed to assess the cracking behavior and to derive the indentation fracture toughness  $K_{\text{IC}}$ . Using a

Vickers Hardness Tester MV-IS instrument (Buehler Ltd, Lake Bluff, USA), Vickers indentations were imprinted at loads of 0.1 kg (0.98 N), 0.2 kg (1.96 N), 0.3 kg (2.94 N) and 0.5 kg (4.9 N). The half-diagonal of the resulting indentations  $a$ , as well as the length of the induced cracks  $l$ , was measured using a laser confocal LEXT OLS6000 microscopy instrument (OLYMPUS, Hamburg, Germany). For the observed Palmqvist crack system with a ratio of  $0.25 \leq l/a \leq 2.5$  [41, 42], the fracture toughness was calculated based on the following Eq. (1) [43, 44]:

$$K_{IC} = 0.035 \left(\frac{l}{a}\right)^{-0.5} \left(\frac{H}{E\Phi}\right)^{-0.4} \left(\frac{Ha^{0.5}}{\Phi}\right) \quad (1)$$

where  $\Phi$  is a constraint factor with a value of 3. The required  $E$  and  $H$  values are based on the micro-indentation measurements performed at the same loads as the fracture toughness tests.

## Results and discussion

The nominal and actual compositions as determined by ICP-OES are shown in Table 2. Considering the limit of experimental instrument uncertainty, the measurement confirms the desired compositions. The  $ZrO_2$  content in the NHSP samples is probably a result of trace amounts being present in the educts.

Figure 1a presents the particle size distributions of the starting powders of the specimens of the NZSP test series. Despite similar synthesis, very different particle size distributions are revealed for the different compositions. While the powders of NZScSP and NZSP 3.0 specimens appear to be very similar, with basically a bimodal distribution and a median particle size ( $D_x(50)$  value) of 2.7  $\mu m$  and 2.8  $\mu m$ , respectively, the NZMgSP starting powder possess a trimodal distribution with larger particles, but also a sub-micron region, resulting in a  $D_x(50)$  of 11  $\mu m$ . The distribution function of NZSP3.6 powder is unimodal with a  $D_x(50)$  of 5.1  $\mu m$ .

The particle size distributions of the starting powders for the NHSP specimens are presented in Fig. 1b. The powders NHSP2.1 and NHSP2.3 are both unimodal, with a median particle size  $D_x(50)$  of 13.5  $\mu m$  and 7.5  $\mu m$ , respectively. The powders of NHSP2.8 and NHSP3.2 both exhibit a bimodal distribution, with a large fraction of fine particles  $\leq 40 \mu m$  and a smaller amount of coarser particles  $> 100 \mu m$ . This bimodal distribution leads

to a median particle size of 6.2  $\mu m$  for NHSP2.8 and 8.7  $\mu m$  for NHSP3.2.

The sintered specimens have been investigated regarding their phase compositions and the corresponding XRD patterns can be found in the supplementary (Figure Sup.1–8). Crystal structures of NHSP and NZSP are reported to be rhombohedral, except for the compositional range of  $1.8 < x < 2.2$ , for which a monoclinic distortion has been reported [45, 46]. However, all specimens investigated in the current work possess independent of their composition a monoclinic C2/c crystal structure.

The XRD patterns clearly indicate the presence of secondary phases, i.e., for NHSP monoclinic  $HfO_2$  and for NZSP monoclinic  $ZrO_2$ . The Rietveld refinement result of the XRD patterns is summarized in Table 3. For the NHSP specimens the “a” as well as “b” lattice parameters depend on the sodium content, as can be seen in Table 3. The formation and amount of the secondary phase  $HfO_2$  appear to be linked to the sodium content. For the NZSP specimens, the same trend can be observed; the specimens with the highest sodium content yield the largest “a” and “b” lattice parameters and exhibit the least amount of the secondary phase  $ZrO_2$ .

The substitution of Mg into the NZSP crystal structure appears to have only a minor influence on the lattice parameters and no effect on the formation of the secondary phase  $ZrO_2$ . The substitution of Sc, on the other hand, leads to larger lattice parameters and seems to hinder the formation of the secondary phase  $ZrO_2$ . Here, the total amount of the secondary phase is  $\sim 1\%$ , compared to  $\sim 5\%$  for the Mg-doped as well as the undoped NZSP.

A number of differences can be observed from the SEM images of the NZSP specimens (Fig. 2). In agreement with the XRD results, the secondary phase  $ZrO_2$  (EDX measurement, Supplementary Figure Sup. 9) can also be observed in the specimen NZSP3.0, NZMgSP and NZScSP by EDX, whereas no secondary phase is present in the specimen NZSP3.6 which has the highest sodium content. Additionally, in the specimen NZSP3.0 a glassy phase engulfing smaller pores can be observed (Fig. 2b), while this phase is not present in the specimens with similar sodium contents NZMgSP and NZScSP.

The formation of a glassy phase in NASICON material has already been reported, being apparently associated with elevated sintering temperatures as well as a low sodium contents [31–33]. For the NHSP

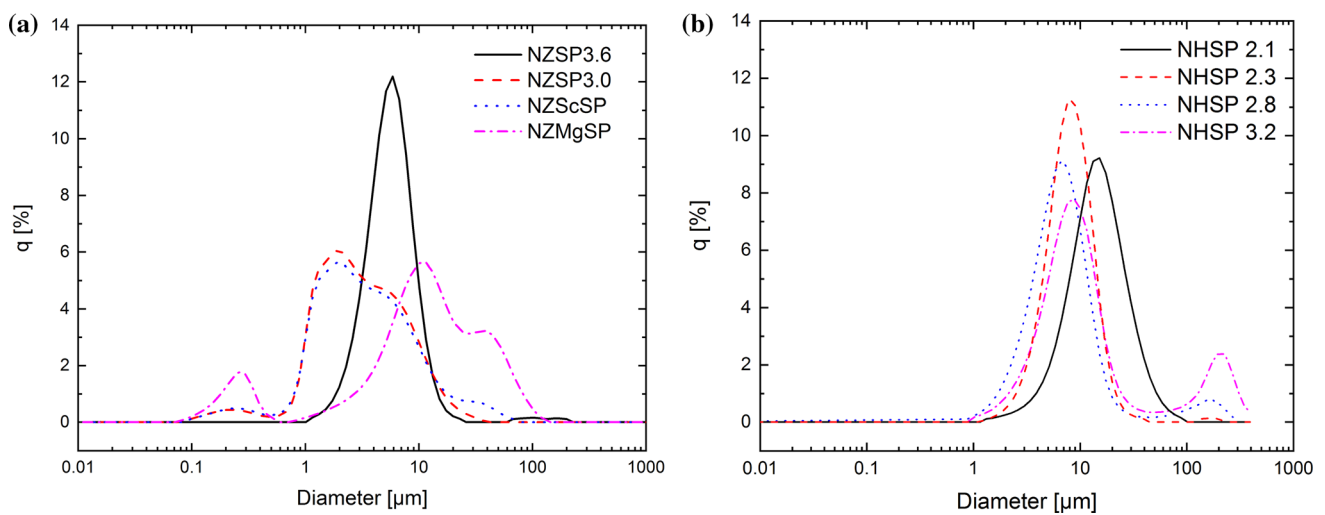
**Table 2** Nominal and actual compositions of the synthesized NASICON specimens as determined by ICP-OES

Starting powder of specimen	Determined composition in mol						
	Na	Sc	Mg	Zr	Si	P	O
NZSP 3.6	3.60 (0.12)	–	–	2.00 (0.07)	2.27 (0.13)	0.64 (0.02)	12
NZSP 3.0	2.99 (0.05)	–	–	2.00 (0.04)	2.26 (0.04)	0.70 (0.01)	11.85
NZScSP	3.15 (0.06)	0.35 (0.01)	–	1.60 (0.02)	1.95 (0.05)	0.93 (0.02)	12
NZMgSP	3.15 (0.07)	–	0.03	1.95 (0.04)	1.99 (0.04)	0.95 (0.02)	12

Starting powder of specimen	Determined composition in mol						
	Na	Hf	Zr	Si	P	O	
NHSP 2.1	2.12 (0.15)	1.90 (0.17)	–	0.1 (0.01)	2.44 (0.19)	0.56 (0.04)	11.35
NHSP 2.3	2.29 (0.07)	1.90 (0.08)	–	0.09 (0.01)	2.48 (0.10)	0.61 (0.04)	11.45
NHSP 2.8	2.82 (0.10)	1.98 (0.08)	–	0.02 (0.01)	2.64 (0.11)	0.59 (0.03)	11.6
NHSP 3.2	3.20 (0.13)	1.91 (0.07)	–	0.09 (0.01)	2.47 (0.08)	0.59 (0.02)	11.85

Compositions are given in mol, uncertainties in terms of the standard deviation are given in brackets. ICP-OES compositions were normalized based on the Zr target value

**Figure 1** Particle size distribution of the powder corresponding to the **a** NZSP series and **b** NHSP series, as measured by laser granulometry.

series, the data summarized in Table 3 confirm that the fraction of a glassy phase increases with decreasing Na content, as does the secondary phase. In the SEM images at lower magnifications (Fig. 3a), hemispherical voids can be observed in NZMgSP and NZSP3.0, while these voids are not present in NZSP3.6 and NZScSP. These voids can be interpreted as bloating, which has been linked to higher sintering temperatures, lower sodium content and the formation of the  $ZrO_2$  secondary phase as well as glassy phase [46, 47]. These effects can mainly be attributed

to incongruent melting of NASICON. The doping with Sc seems to inhibit such effects associated with incongruent melting, since no bloating, no glassy phase formation and only small amounts of secondary phase were observed in the specimen.

SEM images at higher magnification (Fig. 3b) show micro-cracks in the NASICON grains, originating from the  $ZrO_2$  secondary phase formation. These cracks might be a result of the expansion-associated transformation of tetragonal to monoclinic  $ZrO_2$ , that has been described in the literature [47].

**Table 3** Overview of the results obtained for all specimens

label	Crystallographic properties					Microstructural properties				Mechanical properties									
	Space group	a	b	c	$\beta$	Second phase [wt.%]	Glassy phase content [%]	Grain size [ $\mu\text{m}$ ]	Porosity (image) [%]	E [GPa]			H [GPa]		$K_{IC}$	$\sigma$			
		[Å]	[Å]	[Å]	[°]		[%]	[ $\mu\text{m}$ ]	[%]	100 mN	250 mN	500 mN	100 mN	250 mN	500 mN	[MPa $\text{m}^{1/2}$ ]	[mS/cm]		
NZSP 3.6	C2/c	15.73	9.11	9.20	124.3	–	–	1.0 (0.3)	7.8 (0.2)	–	–	77.2 (2.6)	77.0 (1.8)	74.1 (5.2)	5.0 (0.4)	4.9 (0.3)	4.7 (0.5)	2.2 (0.2)	2.7 (0.2)
NZSP 3.0	C2/c	15.68	9.07	9.23	123.9	5	11.6 (0.6)	0.6 (0.1)	3.1 (0.4)	–	–	87.7 (5.9)	87.7 (4.1)	87.8 (6.0)	7.3 (1.2)	7.3 (0.9)	6.9 (1.1)	1.5 (0.3)	1.5 (0.3)
NZScSP	C2/c	15.71	9.08	9.19	124.4	1	–	1.2 (0.3)	4.5 (0.6)	–	–	78.4 (2.9)	73.2 (4.4)	70.8 (4.4)	5.6 (0.3)	4.8 (0.9)	4.8 (0.6)	1.3 (0.2)	1.6 (0.1)
NZMgSP	C2/c	15.66	9.06	9.23	123.8	5	–	0.6 (0.1)	9.1 (0.6)	–	–	82.6 (9.2)	83.0 (6.5)	79.7 (9.1)	5.9 (1.2)	6.0 (1.0)	5.8 (1.2)	1.6 (0.2)	1.2 (0.1)
NHSP 2.1	C2/c	15.52	8.97	9.22	123.8	27	28.6 (3.2)	0.7 (0.1)	8.8 (1.8)	–	–	90.0 (0.9)	81.6 (4.5)	75.1 (6.4)	8.6 (0.5)	7.8 (1.1)	7.3 (1.6)	1.2 (0.1)	0.2 (0.1)
NHSP 2.3	C2/c	15.54	8.98	9.21	123.7	24	23.5 (1.0)	0.6 (0.1)	3.3 (1.2)	–	–	90.0 (2.8)	84.1 (3.2)	79.2 (3.2)	8.8 (0.5)	8.0 (0.5)	7.6 (0.7)	1.5 (0.2)	0.3 (0.1)
NHSP 2.8	C2/c	15.57	9.01	9.21	123.7	13	22.8 (1.2)	0.7 (0.1)	6.1 (3.2)	–	–	85.6 (11)	81.8 (11)	77.0 (15)	7.7 (1.6)	7.6 (2.0)	6.6 (2.3)	1.5 (0.1)	0.9 (0.2)
NHSP 3.2	C2/c	15.61	9.03	9.21	123.8	6	14.3 (2.7)	0.7 (0.1)	1.8 (1.5)	–	–	88.9 (8.1)	88.1 (1.7)	84.6 (4.7)	8.1 (1.5)	7.8 (0.6)	7.4 (0.8)	1.3 (0.1)	2.9 (0.3)

Crystallographic characteristics were obtained by XRD and subsequent Rietveld refinement. The microstructural properties were obtained by image analysis of SEM images of the specimens' surfaces. The porosities were measured by image analysis. The mechanical properties were determined from the indentation experiments. The ionic conductivities were obtained by EIS measurements

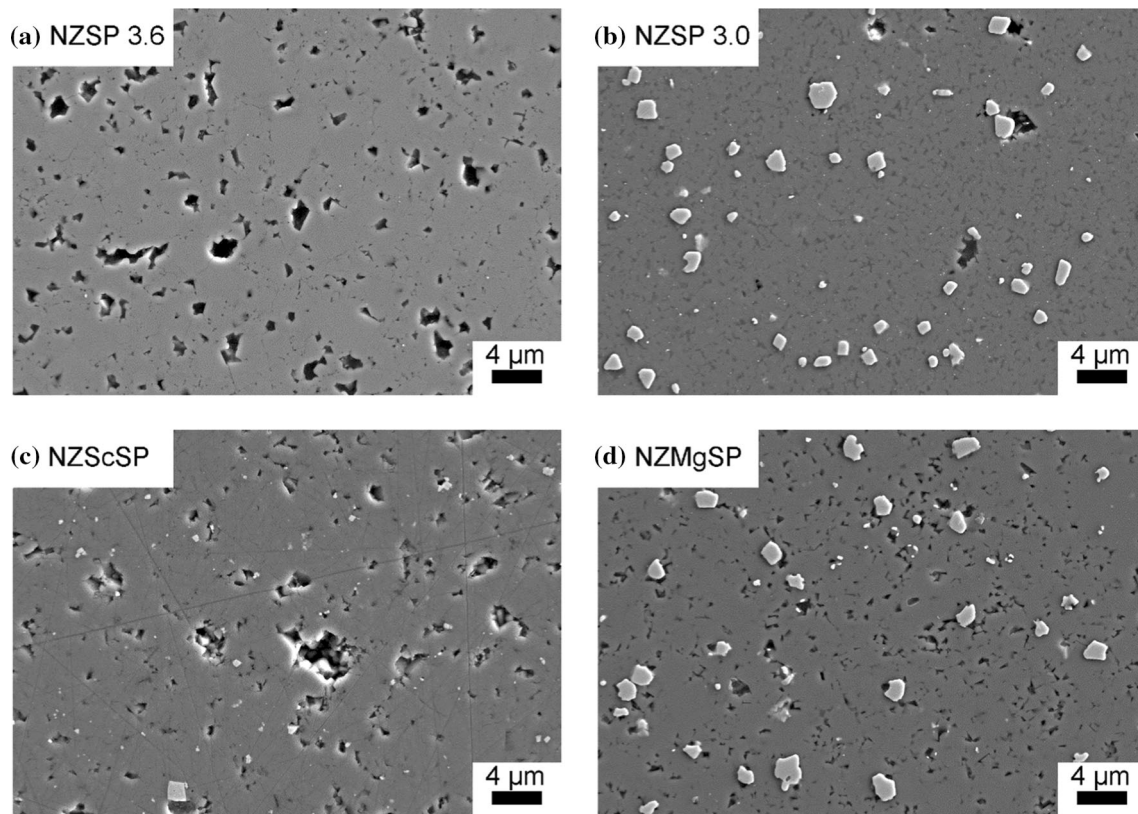


**Figure 2** SEM images of the polished NZSP specimens. Lighter grains are secondary  $ZrO_2$  phases. These can be observed for all specimens, except for NZSP3.6. In NZSP3.0 an additional glassy phase can be observed along the grain boundaries (dark grey). The phases were identified by EDX measurements (see supplementary

Figure Sup. 9). The pore size distribution of the specimens is quite different, was even large, hemispherical voids can be observed at lower magnifications for NZMgSP and NZSP3.0 (see supplementary Figure Sup. 11) but not for the other specimens.

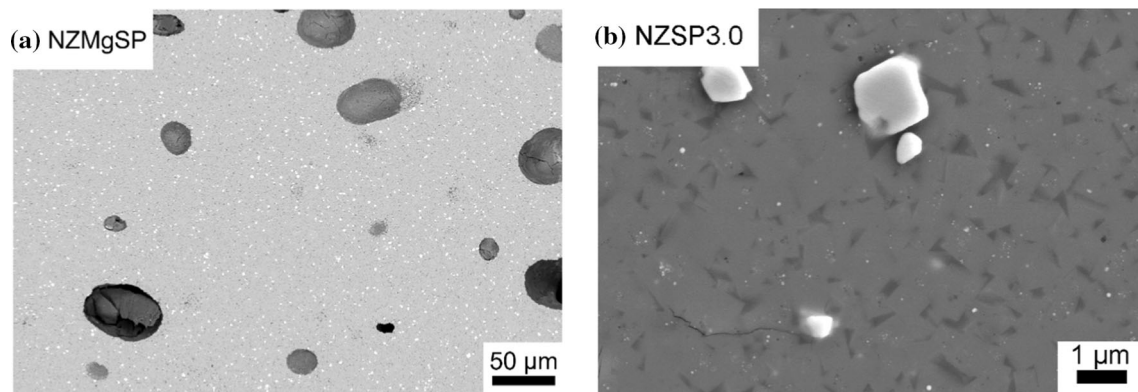


**Figure 3** SEM images of NHSP2.1 at low magnification **a** showing the voids caused by bloating and of NZSP3.0 at high magnification **b** showing cracks originating from the secondary  $ZrO_2$ .

Overall, the microstructures of all NHSP specimens are similar (Fig. 4), where aforementioned effects such as bloating, micro-cracks, a secondary phase (in this case  $HfO_2$ , as confirmed by XRD and EDX) and a

glassy phase can be observed for all NHSP specimens.

Based on the SEM images, grain sizes, glassy phase contents and porosities can be assessed. For the NZSP

specimens denser ceramics are achieved in cases where the starting powders have a lower median particle sizes. However, for the NHSP specimens, the dominating effect seems to be either bloating, leading to large voids or rather the formation of glassy phase filling smaller pores. Therefore, the effect of the particle size distribution of the starting powder on the densification of the sintered NHSP specimens cannot be observed.

The average grain size is similar for the different materials, being  $\sim 0.7 \mu\text{m}$ . An exception is NZScSP, which has a larger grain size of  $\sim 1.2 \mu\text{m}$  possibly related to the low amount of a secondary phase. The same can be observed for NZSP3.6, which also yielded a somewhat larger grain size compared to the other compositions, while no secondary phase content could be detected. In summary, the results show higher amounts of glassy phase, secondary phases, micro-cracks and large semispherical voids with decreasing sodium content for both NZSP and NHSP test series.

For all materials, room temperature ionic conductivities were measured. Due to the very low

impedance of the sample, the induction caused by the internal circuits of the equipment becomes significant and has to be considered by implementing an electromagnetic coil in the equivalent circuit model (Fig. 5) that is used to fit the curve.

Note, it has been reported that the semicircle attributed to the bulk conductivity of  $\text{Na}_{3.4}\text{Zr}_2\text{Si}_{2.4}\text{P}_{0.6}\text{O}_{12}$  cannot be observed at  $25^\circ\text{C}$  in the investigated frequency range [48, 49]. For the purpose of the fit, we therefore consider just a resistance for the first  $x$ -axis intercept. The capacitance values of Q2 ( $3.0 \cdot 10^{-9}$  F) and Q3 ( $3.6 \times 10^{-6}$  F) fit well with characteristic values observed for the grain boundary and the electrolyte–electrode interface. So, R1 and R2 can be estimated to be the bulk and grain boundary resistances, respectively, the sum of which representing the total resistance that is used to calculate the total conductivity.

The resulting total ionic conductivities of all NASICON compositions are listed in Table 3. The values achieved in this work are slightly lower than the ones reported in the literature [48–50]. However, the expected general trend from NZSP3.6, possessing

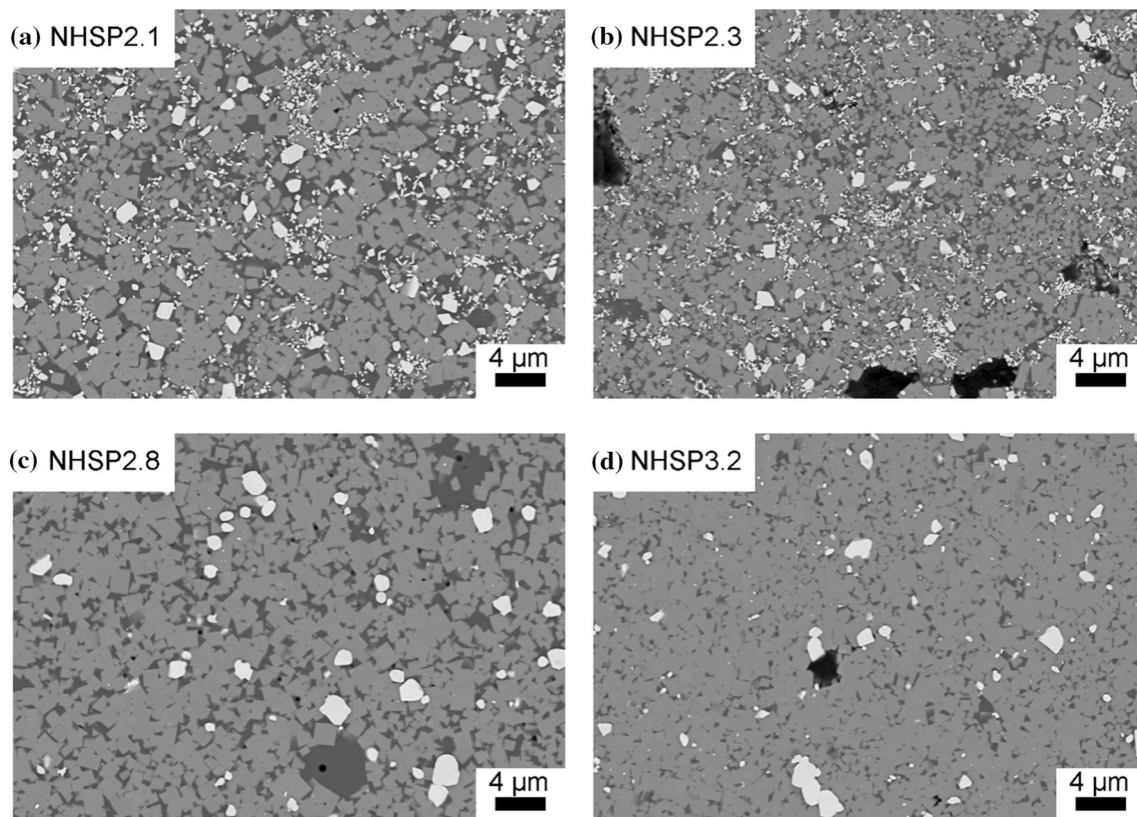


**Figure 4** SEM images of the polished NHSP specimens. In all specimens, secondary  $\text{HfO}_2$  crystals (bright grains) exist as well as a glassy phase (dark grey) at the grain boundaries. The phases were confirmed by EDX analysis (see supplementary, Figure Sup. 10).



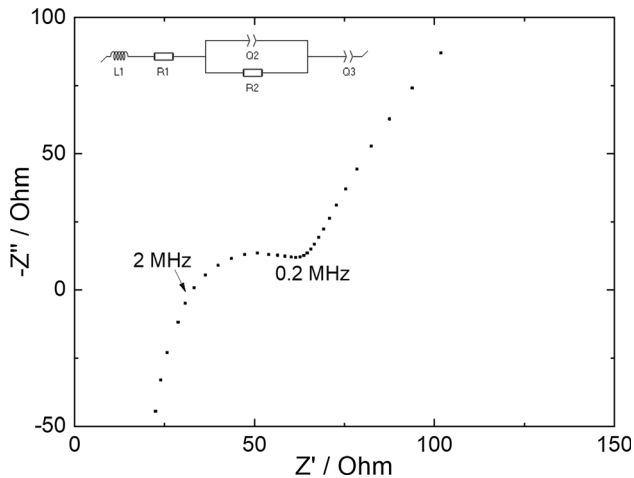


**Figure 5** Nyquist plot of an EIS measurement on sample NZSP3.0, including the equivalent circuit model used to fit the curve.

the highest total ionic conductivity due to the high sodium content, can be confirmed. Observation made above showed the low sodium content is responsible for the appearance and severity of glass phase and also secondary phase; however, higher sodium content also means a higher amount of the charge carrier in the specimens. Therefore, it is unclear if higher conductivity values with enhanced sodium content are related to the higher amount of charge carriers or to the lower amounts of glass and secondary phases.

The indentation test-derived elastic modulus and hardness values are presented in Table 3. In general, the indentation results are comparable to literature values [22] considering corresponding load ranges. The elastic modulus and hardness values of all specimens are rather independent of the applied loads in the investigated load range of 100 to 500 mN. The elastic modulus values at the higher loads appear to be lower for a few specimens, probably a result of indentation crack formation.

The Hf-free materials appear to reveal an effect of the porosity on the mechanical properties, with the specimen NZSP3.0 yielding the highest values corresponding to the lowest porosity. Effects of porosity on mechanical characteristics are widely known [51–55]. The lowest porosity of this test series also corresponds to a microstructure with some glassy phase and secondary phase. Specimens NZSP3.6 and NZScSP have rather low values, almost no secondary phase and at the same time marginally larger grain sizes, but still slightly different Na contents. The increased Na content of NZSP3.6 compared to

NZScSP is not reflected in elastic modulus and hardness. Here, the porosity appears to dominate. For the NHSP series, again, the specimen with the lowest porosity, NZSP3.2, yields the highest elastic moduli, while no differences in the hardness are observed. Increased glassy phase and secondary phase contents did not enhance the values, hence also suggesting that for the Hf-free materials the higher elastic modulus of NZSP3.0 is not a result of such effects.

For the NHSP specimens, the crack-length-to-imprint-diameter ratio is in a range of 0.77 to 0.93, and for the NZSP specimens between 0.53 and 0.78, which is indicative of a Palmqvist crack system for all materials ( $0.25 \leq l/a \leq 2.5$ ) [56]. Typical micrographs of imprints and cracks on the surface after indentation in Fig. 6 show the polished surface of NHSP2.1 and NZSP3.6.

The cracks in all investigated materials propagate along a convoluted straight line indicating a mixture of inter- and transgranular fracture mode. In Fig. 7, SEM micrographs of the crack tips at high magnification are shown. As can be seen in Fig. 7(a), no changes in the crack propagation paths due to the glassy phase can be observed, indicating similar mechanical properties of the glassy and the NASICON phase. Due to the higher elastic modulus of the secondary phase ( $\text{ZrO}_2 \sim 200$  GPa;  $\text{HfO}_2 \sim 150$  GPa), the crack deflects at the secondary phase-NASICON interface as can be seen in Fig. 7(b) [57, 58]. This crack deflection might lead to slightly enhanced fracture toughness results [59].

The fracture toughness values of the samples are compiled in Table 3. Measurements at loads of 0.98, 1.96, 2.94 and 4.9 N yield values that in general agree well within the limits of experimental uncertainty. Thus, overall, the different compositions have similar fracture toughness ranging from 1.2 to 1.6  $\text{MPa}\cdot\text{m}^{1/2}$ . In the literature, a strong link between the glassy phase content and the fracture toughness results was suggested [60, 61]. However, in the current work the glassy phase and NASICON main phase seem to exhibit similar mechanical properties; thus, no influence of the glassy phase content on the mechanical properties of the specimens can be observed. Specimen NZSP3.6 showed a significantly higher value of 2.2  $\text{MPa}\cdot\text{m}^{1/2}$ . Since NZSP3.6 is the composition investigated, which does not exhibit a secondary phase, and since we have shown the existence of micro-cracks within the NASICON phase originating

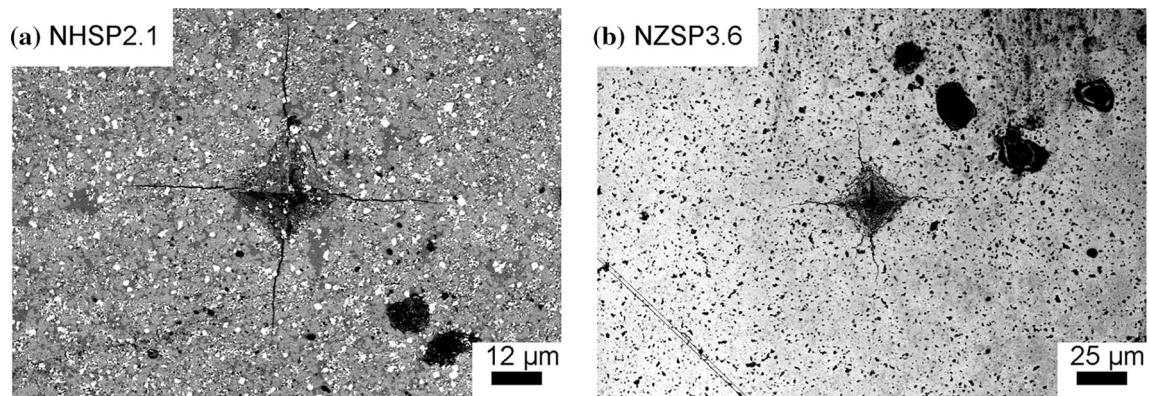


**Figure 6** Laser confocal microscopy images of Vickers imprints obtained at a load of 2.94 N and induced cracks on the surface of specimens a) NHSP2.1 and b) NZSP3.6. The dark spots next to the

imprints in (a) and in (b) are remnants of isopropanol used to clean the surfaces..

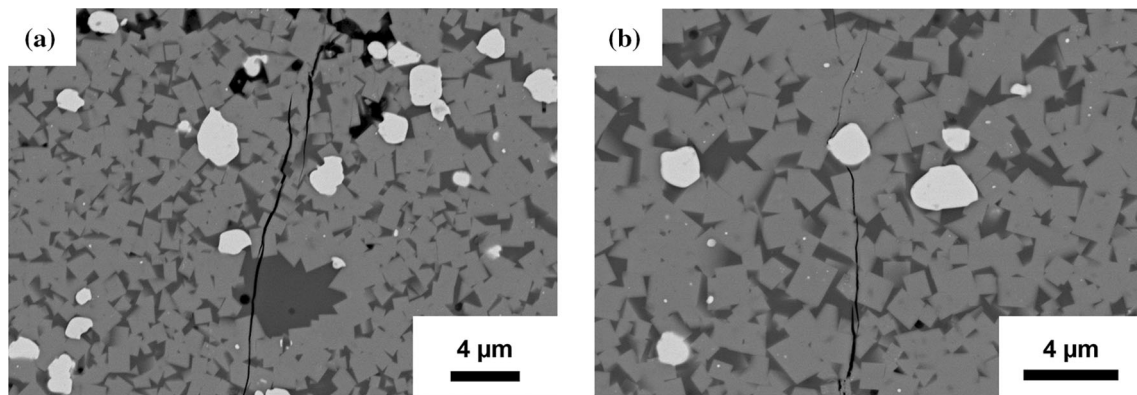


**Figure 7** SEM images of the crack propagation at the tip of the Vickers imprints. **a** Transgranular crack propagation through the NASICON and glass phase. **b** Crack deflection at the NASICON-secondary phase interface.

from the secondary phase, it can be concluded that these micro-cracks in the secondary phase weaken the material and thus reduce the fracture toughness for the other specimens. Note that specimen NZSP3.6 exhibits a rather low hardness; thus, the increased fracture toughness might also be affected by enhanced plastic deformation, but, on the other hand, specimen NZScSP, which has a similar hardness, reveals rather low fracture toughness, thus not confirming this hypothesis. In contrast to the behavior of elastic modulus and hardness, an effect of the porosity on the fracture toughness cannot be observed, perhaps partly related to the chosen indentation positions, which are preferentially located in areas of low porosity, whereas the indentation-derived elastic modulus and hardness values are

averages of rather large data sets of randomly chosen indentation positions.

## Conclusions

Microstructure, conductivity and mechanical properties of NZSP and NHSP specimens with different compositions have been investigated. The densification of the specimens seems to be controlled by the particle size distribution of the starting powders, incongruent melting of the NASICON phase and bloating. However, the incongruent melting of the NASICON phase and the formation of bloating seems to be dominating. The bloating effect creates large voids within the specimens, thus reducing the

relative density. However, a direct relation between the number of voids and the composition could not be found. The incongruent melting leads to the formation of a glassy phase filling micro-pores. The amount of secondary ( $\text{HfO}_2$  and  $\text{ZrO}_2$ ) as well as glassy phase seems to decrease with increasing sodium content. The conductivity depends on the sodium content, with the highest conductivity values for the specimens with the highest sodium content and accompanied by the lowest amount of secondary phase. The secondary phases induce micro-cracks in the materials; thus, it is suggested that this effect is reducing the apparent fracture toughness. The elastic modulus and hardness results of the specimens appear to be affected mainly by the porosity.

Overall in order to improve the fracture toughness and ionic conductivity, the formation of secondary phases and bloating should be inhibited. This might be achieved by higher sodium contents, which should also eliminate the glassy phase content as well as the secondary phase content.

**Supplementary Information:** The online version contains supplementary material available at <http://doi.org/10.1007/s10853-022-08023-9>.

## Acknowledgements

The authors would like to thank Mr. M. Ziegner and Dr. D. Grüner, IEK-2 for the XRD and SEM investigations, respectively, Dr. Y. J. Sohn and Ms. A. Hilgers, IEK-1 for further XRD and PSD investigation, and Mr. V. Nischwitz, ZEA-3 for ICP-OES analysis. We also thank the Helmholtz Association and the Federal Ministry of Education and Research (BMBF) for the funding within the project MiTemp (Grant No. 13XP0183B) and the project ProFeLi (Grant. No. 13XP0184B).

**Open Access** This article is licensed under a Creative Commons Attribution 4.0 International License, which permits use, sharing, adaptation, distribution and reproduction in any medium or format, as long as you give appropriate credit to the original author(s) and the source, provide a link to the Creative Commons licence, and indicate if changes were made. The images or other third party material in this article are included in the article's Creative Commons licence, unless indicated otherwise in a credit line to

the material. If material is not included in the article's Creative Commons licence and your intended use is not permitted by statutory regulation or exceeds the permitted use, you will need to obtain permission directly from the copyright holder. To view a copy of this licence, visit <http://creativecommons.org/licenses/by/4.0/>.

## Funding

Open Access funding enabled and organized by Projekt DEAL.

**Supplementary Information:** The online version contains supplementary material available at <http://doi.org/10.1007/s10853-022-08023-9>.

## References

- [1] Palomares V, Serras P, Villaluenga I, Hueso KB, Carretero-González J, Rojo T (2012) Na-ion batteries, recent advances and present challenges to become low cost energy storage systems. *Energy Environ Sci* 5(3):5884–5901
- [2] Tarascon J-M, Armand M (2011) Issues and challenges facing rechargeable lithium batteries. *Materials for sustainable energy: a collection of peer-reviewed research and review articles from Nature Publishing Group*, pp. 171–179
- [3] Armand M, Tarascon J-M (2008) Building better batteries. *Nature* 451(7179):652–657
- [4] Chen R, Li Q, Yu X, Chen L, Li H (2019) Approaching practically accessible solid-state batteries: stability issues related to solid electrolytes and interfaces. *Chem Rev* 120(14):6820–6877
- [5] Wang Q, Ping P, Zhao X, Chu G, Sun J, Chen C (2012) Thermal runaway caused fire and explosion of lithium ion battery. *J Power Sour* 208:210–224
- [6] Slater MD, Kim D, Lee E, Johnson CS (2013) Sodium-ion batteries. *Adv Func Mater* 23(8):947–958
- [7] Ellis BL, Nazar LF (2012) Sodium and sodium-ion energy storage batteries. *Curr Opin Solid State Mater Sci* 16(4):168–177
- [8] Tian H, Liu S, Deng L, Wang L, Dai L (2021) New-type Hf-based NASICON electrolyte for solid-state Na-ion batteries with superior long-cycling stability and rate capability. *Energy Storage Mater* 39:232–238
- [9] Lu Y, Li L, Zhang Q, Niu Z, Chen J (2018) Electrolyte and interface engineering for solid-state sodium batteries. *Joule* 2(9):1747–1770

- [10] Hong H-P (1976) Crystal structures and crystal chemistry in the system  $\text{Na}1+x\text{Zr}_2\text{SixP}_3-x\text{O}_{12}$ . *Mater Res Bull* 11(2):173–182
- [11] Wang X, Liu Z, Tang Y, Chen J, Wang D, Mao Z (2021) Low temperature and rapid microwave sintering of  $\text{Na}_3\text{Zr}_2\text{Si}_2\text{PO}_{12}$  solid electrolytes for Na-Ion batteries. *J Power Sour* 481:228924
- [12] Goodenough JB, Hong H-P, Kafalas J (1976) Fast  $\text{Na}^{+}$ -ion transport in skeleton structures. *Mater Res Bull* 11(2):203–220
- [14] Noguchi Y, Kobayashi E, Plashnitsa LS, Okada S, Yamaki J-I (2013) Fabrication and performances of all solid-state symmetric sodium battery based on NASICON-related compounds. *Electrochim Acta* 101:59–65
- [15] Ahmad A, Wheat T, Kuriakose A, Canaday J, McDonald A (1987) Dependence of the properties of Nasicons on their composition and processing. *Solid State Ionics* 24(1):89–97
- [16] Shao Y et al (2019) A novel NASICON-based glass-ceramic composite electrolyte with enhanced Na-ion conductivity. *Energy Storage Mater* 23:514–521
- [17] Qie Y, Wang S, Fu S, Xie H, Sun Q, Jena P (2020) Yttrium–sodium halides as promising solid-state electrolytes with high ionic conductivity and stability for Na-ion batteries. *J Phys Chem Lett* 11(9):3376–3383
- [18] Jolley AG, Cohn G, Hitz GT, Wachsman ED (2015) Improving the ionic conductivity of NASICON through aliovalent cation substitution of  $\text{Na}_3\text{Zr}_2\text{Si}_2\text{PO}_{12}$ . *Ionics* 21(11):3031–3038
- [19] Wang C et al (2021) Grain Boundary design of solid electrolyte actualizing stable all-solid-state sodium batteries. *Small* 17(40):2103819
- [20] Li W, Zhao N, Bi Z, Guo X (2022) Insight into synergetic effect of bulk doping and boundary engineering on conductivity of NASICON electrolytes for solid-state Na batteries. *Appl Phys Lett* 121(3):033901
- [21] Ran L et al (2021) Sc, Ge co-doping NASICON boosts solid-state sodium ion batteries' performance. *Energy Storage Mater* 40:282–291
- [22] Nonemacher JF, Naqash S, Tietz F, Malzbender J (2019) Micromechanical assessment of Al/Y-substituted NASICON solid electrolytes. *Ceram Int* 45(17):21308–21314
- [23] Famprikis T, Canepa P, Dawson JA, Islam MS, Masquelier C (2019) Fundamentals of inorganic solid-state electrolytes for batteries. *Nat Mater* 18:1–14
- [24] Tsai C-L et al (2020) Dendrite-tolerant all-solid-state sodium batteries and an important mechanism of metal self-diffusion. *J Power Sour* 476:228666
- [25] Zhang W et al (2018) Degradation mechanisms at the  $\text{Li}_{10}\text{GeP}_2\text{S}_{12}/\text{LiCoO}_2$  cathode interface in an all-solid-state lithium-ion battery. *ACS Appl Mater Interfaces* 10(26):22226–22236
- [26] Zhang F et al (2020) A review of mechanics-related material damages in all-solid-state batteries: mechanisms, performance impacts and mitigation strategies. *Nano Energy* 70:104545
- [27] Raj R, Wolfenstine J (2017) Current limit diagrams for dendrite formation in solid-state electrolytes for Li-ion batteries. *J Power Sour* 343:119–126
- [28] Lu X, Xia G, Lemmon JP, Yang Z (2010) Advanced materials for sodium-beta alumina batteries: status, challenges and perspectives. *J Power Sour* 195(9):2431–2442
- [29] Jalalian-Khakhshour A, Phillips C, Jackson L, Dunlop T, Margadonna S, Deganello D (2020) Solid-state synthesis of NASICON ( $\text{Na}_3\text{Zr}_2\text{Si}_2\text{PO}_{12}$ ) using nanoparticle precursors for optimisation of ionic conductivity. *J Mater Sci* 55(6):2291–2302. <https://doi.org/10.1007/s10853-019-0416-2>
- [30] Lee S-M, Lee S-T, Lee D-H, Lee S-H, Han S-S, Lim S-K (2015) Effect of particle size on the density and ionic conductivity of  $\text{Na}_3\text{Zr}_2\text{Si}_2\text{PO}_{12}$  NASICON. *J Ceram Process Res* 16(1):49–53
- [31] Fuentes R, Figueiredo F, Marques F, Franco J (2002) Optimised NASICON ceramics for  $\text{Na}^{+}$  sensing. *Ionics* 8(5):383–390
- [32] Kuriakose A, Wheat T, Ahmad A, Dirocco J (1984) Synthesis, sintering, and microstructure of NASICONs. *J Am Ceram Soc* 67(3):179–183
- [33] Khakpour Z (2016) Influence of M:  $\text{Ce}^{4+}$ ,  $\text{Gd}^{3+}$  and  $\text{Yb}^{3+}$  substituted  $\text{Na}_{3+x}\text{Zr}_{2-x}\text{M}_x\text{Si}_2\text{PO}_{12}$  solid NASICON electrolytes on sintering, microstructure and conductivity. *Electrochim Acta* 196:337–347
- [34] Holzapfel M, Wilde D, Hupbauer C, Ahlbrecht K, Berger T (2017) Medium-temperature molten sodium batteries with aqueous bromine and iodine cathodes. *Electrochim Acta* 237:12–21
- [35] Shimizu Y, Azuma Y, Michishita S (1997) Sol–gel synthesis of NASICON discs from aqueous solution. *J Mater Chem* 7(8):1487–1490
- [36] Ma Q, Guin M, Naqash S, Tsai C-L, Tietz F, Guillon O (2016) Scandium-substituted  $\text{Na}_3\text{Zr}_2(\text{SiO}_4)_2(\text{PO}_4)$  prepared by a solution-assisted solid-state reaction method as sodium-ion conductors. *Chem Mater* 28(13):4821–4828
- [37] de Boer GB, de Weerd C, Thoenes D, Goossens HW (1987) Laser diffraction spectrometry: Fraunhofer diffraction versus Mie scattering. *Part Part Syst Charact* 4(1–4):14–19
- [38] Schneider CA, Rasband WS, Eliceiri KW (2012) NIH Image to ImageJ: 25 years of image analysis. *Nat Methods* 9(7):671–675

- [39] Schiebold K (2014) Durchführung von Eindringprüfungen. In: Zerstörungsfreie Werkstoffprüfung-Eindringprüfung: Springer. pp. 107–125
- [40] Deng Z, Wang Z, Chu I-H, Luo J, Ong SP (2016) Elastic properties of alkali superionic conductor electrolytes from first principles calculations. *J Electrochem Soc* 163(2):A67–A74
- [41] Ponton C, Rawlings R (1989) Vickers indentation fracture toughness test Part 2 Application and critical evaluation of standardised indentation toughness equations. *Mater Sci Technol* 5(10):961–976
- [42] Ponton CB, Rawlings RD (1989) Vickers indentation fracture toughness test Part 1 Review of literature and formulation of standardised indentation toughness equations. *Mater Sci Technol* 5(9):865–872
- [43] Niihara K, Morena R, Hasselman D (1982) Evaluation of  $K_{Ic}$  of brittle solids by the indentation method with low crack-to-indent ratios. *J Mater Sci Lett* 1(1):13–16
- [44] Niihara K (1983) A fracture mechanics analysis of indentation-induced Palmqvist crack in ceramics. *J Mater Sci Lett* 2(5):221–223
- [45] Vogel E, Cava R, Rietman E (1984) Na<sup>+</sup> ion conductivity and crystallographic cell characterization in the Hf-nasicon system Na<sub>1+x</sub>Hf<sub>2</sub>Si<sub>x</sub>P<sub>3-x</sub>O<sub>12</sub>. *Solid State Ionics* 14(1):1–6
- [46] Fuentes R, Figueiredo F, Marques F, Franco J (2001) Influence of microstructure on the electrical properties of NASICON materials. *Solid State Ionics* 140(1–2):173–179
- [47] McENTIRE BJ, Bartlett R, Miller G, Gordon R (1983) Effect of decomposition on the densification and properties of nasicon ceramic electrolytes. *J Am Ceram Soc* 66(10):738–742
- [48] Ma Q, Tsai C-L, Wei X-K, Heggen M, Tietz F, Irvine JT (2019) Room temperature demonstration of a sodium superionic conductor with grain conductivity in excess of 0.01 S cm<sup>-1</sup> and its primary applications in symmetric battery cells. *J Mater Chem A* 7(13):7766–7776
- [49] Kehne P et al (2019) Sc-substituted Nasicon solid electrolyte for an all-solid-state Na<sub>x</sub>CoO<sub>2</sub>/Nasicon/Na sodium model battery with stable electrochemical performance. *J Power Sour* 409:86–93
- [50] Samiee M et al (2017) Divalent-doped Na<sub>3</sub>Zr<sub>2</sub>Si<sub>2</sub>PO<sub>12</sub> natrium superionic conductor: Improving the ionic conductivity via simultaneously optimizing the phase and chemistry of the primary and secondary phases. *J Power Sour* 347:229–237
- [51] Magdeski J (2010) The porosity dependence of mechanical properties of sintered alumina. *J Univ Chem Technol Metall* 45(2):143–148
- [52] Wang JC (1984) Young's modulus of porous materials. *J Mater Sci* 19(3):801–808. <https://doi.org/10.1007/BF00540451>
- [53] Phani KK, Niyogi S (1987) Young's modulus of porous brittle solids. *J Mater Sci* 22(1):257–263. <https://doi.org/10.1007/BF01160581>
- [54] Fryxell R, Chandler B (1964) Creep, strength, expansion, and elastic moduli of sintered BeO as a function of grain size, porosity, and grain orientation. *J Am Ceram Soc* 47(6):283–291
- [55] Ramakrishnan N, Arunachalam V (1990) Effective elastic moduli of porous solids. *J Mater Sci* 25(9):3930–3937. <https://doi.org/10.1007/BF00582462>
- [56] Bamzai K, Kotru P, Wanklyn B (2000) Fracture mechanics, crack propagation and microhardness studies on flux grown ErAlO<sub>3</sub> single crystals. *J Mater Sci Technol* 16(4):405–410
- [57] Vargas ALM, de Araújo Ribeiro F, Hübler R (2015) Changes in the Young modulus of hafnium oxide thin films. *Nucl Instrum Methods Phys Res Sect B Beam Interact Mater Atoms* 365:362–366
- [58] Shackelford JF, Alexander W (2000) CRC materials science and engineering handbook. CRC Press, Boca Raton
- [59] Faber KT, Evans AG (1983) Crack deflection processes—I. Theory. *Acta Metall* 31(4):565–576
- [60] Kalnaus S et al (2021) Effect of composition on mechanical properties and conductivity of the dual-ion conductor Na<sub>1+x</sub>Mn<sub>x/2</sub>Zr<sub>2-x/2</sub>(PO<sub>4</sub>)<sub>3</sub> for solid-state batteries. *ACS Appl Energy Mater* 4(10):11684–11692
- [61] Wolfenstine J, Go W, Kim Y, Sakamoto J (2022) Mechanical properties of NaSICON: a brief review. *Ionics*. 1–8

**Publisher's Note** Springer Nature remains neutral with regard to jurisdictional claims in published maps and institutional affiliations.